Raman spectroscopic properties and Raman identification of CaS-MgS-MnS-FeS-Cr 2 FeS 4 sulfides in meteorites and reduced sulfur-rich systems

Caroline Avril, Valérie Malavergne, Razvan Caracas, Brigitte Zanda, Bruno Reynard, Émeline Charon, Ema Bobocioiu, Fabrice Brunet, Stephan Borensztajn, Sylvain Pont, et al.

The Meteoritical Society

Meteoritics & Planetary Science 48, Nr 8, 1415–1426 (2013)
doi: 10.1111/maps.12145

Raman spectroscopic properties and Raman identification of CaS-MgS-MnS-FeS-Cr_2FeS_4 sulfides in meteorites and reduced sulfur-rich systems

Caroline AVRIL[1], Valérie MALAVERGNE[1*], Razvan CARACAS[2], Brigitte ZANDA[3], Bruno REYNARD[2], Emeline CHARON[4], Ema BOBOCIOIU[2], Fabrice BRUNET[5], Stephan BORENSZTAJN[6], Sylvain PONT[3], Martine TARRIDA[1], and François GUYOT[7]

[1]Université Paris Est-Marne La Vallée, Laboratoire des Géomatériaux et Environnement, Champs-sur-Marne, 77454 Cedex, France
[2]Laboratoire de Géologie, ENS Lyon-CNRS15 parvis des Italiens, 69342 Lyon Cedex 07, France
[3]Muséum National d'Histoire Naturelle & CNRS UMR7202, 61 rue Buffon, 75005 Paris, France
[4]Laboratoire de Géologie, Ecole normale supérieure-CNRS, 24 rue Lhomond, 75005 Paris, France
[5]ISTerre-CNRS, Université de Grenoble 1, 1381, rue de la Piscine BP 53, 38041 Grenoble Cedex 9, France
[6]Laboratoire d'Interface et Systèmes Electrochimiques, UPR15 CNRS, 4 place Jussieu, 75252 Paris, France
[7]IMPMC/IPGP, UMR 7590 CNRS, 4 place Jussieu, 75252 Paris, France
[*]Corresponding author. E-mail: malaverg@univ-mlv.fr

(Received 27 November 2011; revision accepted 16 May 2013)

Abstract–Raman spectra were acquired on a series of natural and synthetic sulfide minerals, commonly found in enstatite meteorites: oldhamite (CaS), niningerite or keilite ((Mg,Fe)S), alabandite (MnS), troilite (FeS), and daubreelite (Cr_2FeS_4). Natural samples come from three enstatite chondrites, three aubrites, and one anomalous ungrouped enstatite meteorite. Synthetic samples range from pure endmembers (CaS, FeS, MgS) to complex solid solutions (Fe, Mg, Ca)S. The main Raman peaks are localized at 225, 285, 360, and 470 cm^{-1} for the Mg-rich sulfides; at 185, 205, and 285 cm^{-1} for the Ca-rich sulfides; at 250, 370, and 580 cm^{-1} for the Mn-rich sulfides; at 255, 290, and 365 cm^{-1} for the Cr-rich sulfides; and at 290 and 335 cm^{-1} for troilite with, occasionally, an extra peak at 240 cm^{-1}. A peak at 160 cm^{-1} is present in all Raman spectra and cannot be used to discriminate between the different sulfide compositions. According to group theory, none of the cubic monosulfides oldhamite, niningerite, or alabandite should present first-order Raman spectra because of their ideal rocksalt structure. The occurrence of broad Raman peaks is tentatively explained by local breaking of symmetry rules. Measurements compare well with the infrared frequencies calculated from first-principles calculations. Raman spectra arise from activation of certain vibrational modes due to clustering in the solid solutions or to coupling with electronic transitions in semiconductor sulfides.

INTRODUCTION

Recently, particular effort was put into understanding the occurrence of sulfur-rich phases in magmatic systems and meteorites as well as in material science and metallurgy (e.g., Sinyakavo and Kosyakov 2001; Holzheid and Grove 2002; Keil 2007; Liu et al. 2007). The degassing of sulfur from volcanoes plays an important role in the present and past atmosphere properties, and in the geochemical cycle of sulfur in the Earth system (e.g., Farquhar et al. 2002; Moretti and Ottonello 2005; Liu et al. 2007). Sulfur can take a large number of oxidation states, from 2− to 6+, and it occurs in several gaseous and crystallized forms. Because of this large range of possible oxidation states, it remains a difficult element to study.

The sulfide compounds are important phases in meteorites (e.g., Keil 1989, 2007). Specifically, the major part of sulfur in meteorites is found either in troilite; FeS; or in other sulfides like oldhamite, CaS,

niningerite, MgS, keilite, $(Fe_{>0.5},Mg_{<0.5})S$, alabandite, MnS, and daubreelite, Cr_2FeS_4 (e.g., Keil 1968, 1989, 2010; Lauretta et al. 1997). Troilite is the most common and abundant form of sulfide in meteorites. It has a NiAs-type structure (B8, space group $P6_3/mmc$) with both Fe and S atoms in six-fold coordination (e.g., Farrell et al. 2002). The monosulfide series XS (where X is Ca, Mg, or Mn) is almost exclusively found in enstatite meteorites, which are the most reduced naturally occurring samples from the solar system (Keil 1968). The XS phases are ionic monosulfides with the halite structure (B1, space group *Fm3 m*), with both S^{2-} and X^{2+} in ideal octahedral coordination. Natural monosulfides form complex solid solutions; Ca, Mg, Mn, and Fe being the major substituting cations (e.g., Keil 1968; Skinner and Luce 1971). These compounds are also proposed to have been important in solar nebula (e.g., Lauretta et al. 1997; Pasek et al. 2005), and are equally important for the mineralogy and petrology of the mantles of the Earth and other planets (e.g., Siebert et al. 2004; Gaillard and Scaillet 2009). In spite of their geochemical, planetary, and cosmochemical importance, these sulfides have not yet been fully characterized and, in particular, no Raman data are available.

Raman spectroscopy provides information on the vibrations of atoms in matter and can be used as a fingerprint of structure and composition, for phase identification. Raman spectroscopy is easy to carry out, as it requires little sample preparation, is fast, and generally nondestructive. Raman spectroscopy has found many applications in mineralogy and geochemistry (e.g., McMillan and Hofmeister 1988; Wang et al. 1999; White 2009), but also in material sciences in general (e.g., Soong and Farmer 1978; Toplis and Reynard 2000; Weber and Merlin 2000). In this work, we recorded and calculated Raman and vibrational properties of a series of sulfides found in meteorites to provide a reference database for identification purposes.

The effect on the Raman spectra of sulfides of cation Mg, Ca, Mn, Fe, or Cr substitution in the metal site is discussed. Finally, we propose a scheme for the identification of these sulfides based on Raman spectra. We investigated both natural and synthetic samples. Indeed, enstatite meteorites contain large grains of sulfides, but these grains can easily be altered and they show compositional gradients. We thus synthesized homogeneous samples from powders of pure CaS, MnS, FeS, and Cr_2S_3. Solid solutions of (Fe, Mg, Ca)S were also obtained under high-pressure and high-temperature conditions. Finally, the Raman spectra of several compositions obtained along the MgS-CaS join were modeled based on first-principles calculations.

NATURAL AND SYNTHETIC SAMPLES

Natural Samples

We studied several enstatite meteorites: enstatite chondrites (EC) and achondrites (aubrites), as well as ungrouped meteorites, which have anomalous characteristics (e.g., Keil 1968, 1989; Sears et al. 1982; Kong et al. 1997; Patzer et al. 2001). The mineralogy of EC is dominated by an almost FeO-free enstatite along with Si-bearing kamacite and with troilite. Many different minor sulfides are also present such as oldhamite, niningerite, keilite, alabandite, and daubreelite. Aubrites, like EC, mainly consist of almost FeO-free enstatite along with kamacite and troilite and additional sulfides (like in EC). Enstatite in aubrites underwent igneous processes, which suggested that ECs could be precursors of aubrites (e.g., Keil 1989; McCoy et al. 1999). Some enstatite meteorites show intermediate chemical and textural characteristics between EC and aubrites. They share characteristics with EC (like EL, chondrites with low metal contents), whereas their textures reveal similarities to aubrites (Patzer et al. 2001, 2002). These anomalous meteorites have been classified as ungrouped enstatite-rich meteorites (Grossmann 2000; Grossmann and Zipfel 2001).

Seven polished sections of enstatite meteorites from the Muséum National d'Histoire Naturelle (Paris, France) were studied (Table 1): three EC, three aubrites, and one anomalous enstatite chondrite. Petrographic study by optical and electron microscopies revealed large sulfide-rich areas (Fig. 1). The details (names and types) of these meteorites are given in Table 1.

Synthetic Samples

We used synthetic powders (Goodfellow^{TM}) of CaS, MnS, FeS, and Cr_2S_3 with purities of over 99.99%. We also synthesized several samples along the (Fe,Mg,Ca)S solid solution using an end-loaded and a nonend-loaded piston-cylinder apparatus (at the Ecole normale supérieure, Paris, France, and at the NASA Johnson Space Center, Houston, Texas, USA, respectively). The starting materials were loaded in graphite capsules, which were inserted into conventional high-pressure assemblies consisting of Pyrex-talc or $BaCO_3$ as pressure transmitting medium (e.g., McDade et al. 2002) with MgO internal parts. A graphite heater was used and temperatures were measured with $Pt/PtRh_{10}$ or $W_5Re/W_{26}Re$ thermocouple, separated from the graphite capsule by an alumina or a graphite disc. Details of these presses are given in Musselwhite et al. (2006), Filiberto et al. (2008), and Brunet et al. (2003).

Table 1. Names and type of the enstatite meteorites used in this study. EL means EC with low metal contents and EH means EC with high metal abundances.

Meteorite	Type	Observed sulfides in the section
Saint Sauveur	EH5	Troilite, alabandite, daubreelite, oldhamite, keilite
El Atchane	EL6	Troilite, alabandite, daubreelite, oldhamite
Sahara 97158	EH3	Troilite, alabandite, daubreelite, oldhamite, niningerite
Aubres	Aubrite	Troilite, alabandite, oldhamite
Bustee	Aubrite	Troilite, alabandite, daubreelite, oldhamite
Pesyanoe	Aubrite	Troilite, alabandite, daubreelite, oldhamite
Zakłodzie	Anomalous enstatite meteorite	Troilite, ferro-alabandite

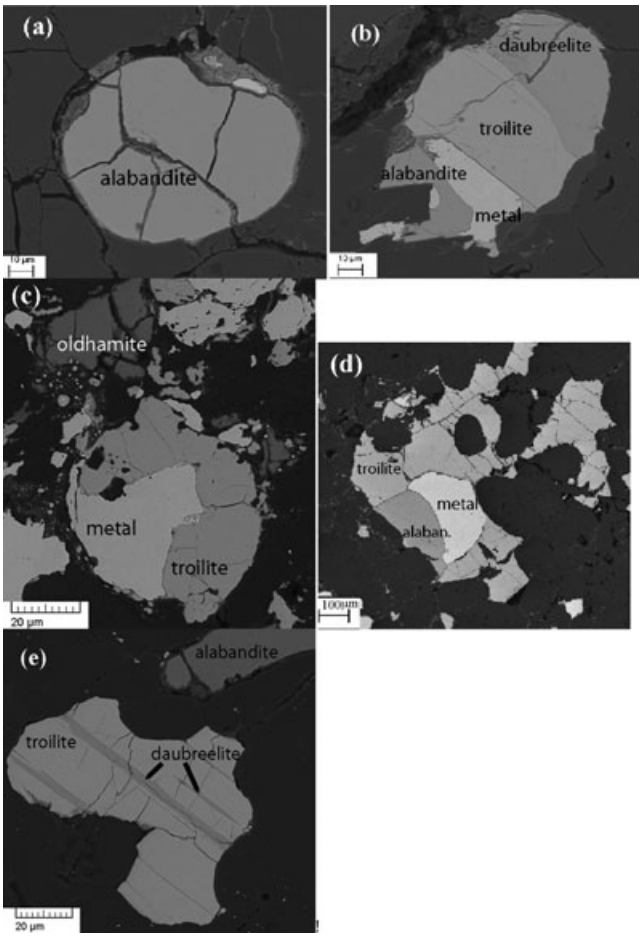

Fig. 1. SEM images in backscattered electron mode showing (a) a grain of alabandite in the silicate matrix in Bustee, (b) an association of different sulfides (daubreelite, troilite, alabandite) with kamacite in Bustee, grains of oldhamite in close association with troilite and metal (c) in Sahara 97158 and (d) in Zaklodzie, (e) lamellar exsolutions of daubreelite in troilite in El Atchane.

Various sulfide textures were generated using different cooling rates to bring the sample down to room temperature as summarized in Table 2. Fast sample cooling (quench) was achieved by switching off the electrical power. Alternatively, the cooling rate was controlled by setting a temperature ramp. Samples were then decompressed, mounted in epoxy, sliced, and polished for analysis. Further experimental details are given in Malavergne et al. (2012).

Table 2. Summary of the experimental conditions for the piston-cylinder runs.

Sample	P (GPa)	T (°C)	Duration	Observed phases
#151	1	1450	1 h 40 min	Met-LS-px-sulf
#154	1	1300	2 h	Met-px-sulf
#ENS 3-2	1	1200	7 days	SiO_2-px-sulf-Met
#ENS 3-1	1	1200	7 days	SiO_2-px-sulf-Met
#ENS 3-3	1	1200	7 days	Pure MgS- Fe
#ENS 180	0.8	1000	3 days	pure CaS
#ENS 184	0.8	800	3 days	pure FeS
#ENS 1	1	1000	6 days	SiO_2-px-sulf-Met
#ENS 204	0.8	1200	10 days	SiO_2-px-sulf-Met
#170	1	1400(1)	150 min[a]	Met-SL- sulf-px
#ENS 5-1	1	1200 (2)	7 days[b]	SiO_2-px-sulf-Met
#ENS 5-2	1	1200 (2)	7 days[b]	SiO_2-px-sulf-Met

Met: metal; LS: quenched liquid silicate; Px: pyroxene.
[a]Sulf: (Mg,Ca,Fe)S and/or FeS. (a) 1 h at 1700 °C followed by a cooling ramp of 110 min down to 1400 °C. (b) 96 h at 1200 °C followed by a cooling ramp of 66 h down to 610 °C.
Experimental details are given in Malavergne et al. (2007).

In another set of experiments, assemblages of silicate glass, with simplified CI chondrite composition (50.8 wt% SiO_2, 3.7 wt% Al_2O_3, 6.2 wt% FeO, 36.3 wt% MgO, 3 wt% CaO, e.g., Malavergne et al. 2007), troilite FeS, and metallic Si (Goodfellow™ > 99.99% purity grade) were used as starting materials. These compounds were ground together to a fine powder (<5 µm) in acetone using an agate mortar and a pestle. Samples are described in detail in Malavergne et al. (2012), and their pressure temperature conditions are summarized in Table 2. Typical textures of the samples are shown in Fig. 2. MgS was synthesized at high pressure by reacting FeS and Mg powders to yield MgS and Fe (Table 2). We also ran pure CaS and pure FeS powders in the piston cylinder (Table 2) to obtain single phases yielding higher Raman-signal quality.

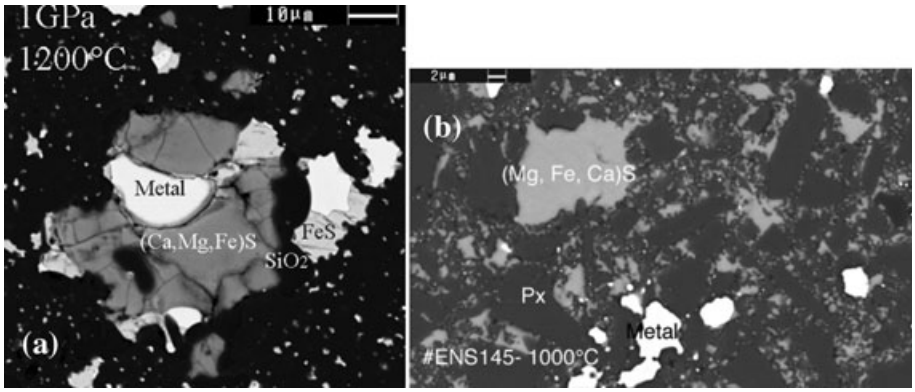

Fig. 2. SEM images (BSE) showing (a) grains of (Ca,Mg,Fe)S in contact with metal and troilite in #ENS3-2, (b) grains of (Ca, Mg,Fe)S in the silicate matrix of #ENS145.

ANALYTICAL AND SIMULATION METHODS

Scanning Electron Microscopy (SEM) and Electron Probe Microanalyzer

Polished natural and synthetic samples were carbon-coated, and then characterized by SEM (ultra55, Zeiss) operating at 15 kV. CAMECA SX-50 and SX-100 electron probe microanalyzers (EPMA) were used to further analyze the samples. Four crystal monochromators detected the first-order reflection of Kα, Mα, or Mβ emission lines: TAP for Mg, Al, Si, PET for Ca, S, and LIF for Fe. The counting times for the major elements were 10 or 20 s and a typical beam current of 10 nA was used at 15 kV with a minimum spot size of 1 μm. Trace elements were analyzed with a longer counting time (120 s) under beam conditions of 40 nA and 15 kV. The standards were Fe_2O_3 for Fe; clinopyroxene for Si, Ca, and Mg; orthoclase for Al; $MnTiO_3$ for Mn; pyrite for S; Cr_2O_3 for Cr; and V_2O_3 for V. The errors in compositions given in Tables 3 and 4 were less than 3% for major elements and generally less than 15% for minor elements.

Raman Spectroscopy

Raman microspectrometry was performed at ambient conditions using a Renishaw INVIA spectrometer equipped with an Ar laser source (514.5 nm), focused through a Leica (×50) magnification objective. The combination with an optical microscope allowed an accurate analysis of the sulfide phases as the incident laser beam had a focused spot size of about 1 μm^2. Raman spectra were collected with 90–960 s acquisition times in the frequency range 70–1000 cm^{-1}. To avoid heating effects, a very low laser incident power of 2 mW was used, leading to a laser power density of about 2.5 mW μm^{-2}. The Rayleigh scattering component was removed by a Notch filter, and the Raman-scattered light was dispersed by a holographic grating with 1800 lines/mm and detected by a CCD camera. Two other Raman spectrometers were also used, T64000 Jobin-Yvon-Horiba equipped with an Ar laser source Coherent and LabRam HR800 Jobin-Yvon equipped with an Ar laser source Spectra-Physics 2018. Raman spectra were collected under the same conditions. During all Raman measurements, we took great care to check that sulfides were not damaged by laser heating. Unfortunately, the pure synthetic powder of MnS oxidized into hausmannite Mn_3O_4 under the laser beam, even under very low laser power (0.1% of its maximum power) showing the great reactivity of this powder. For all the sulfides but MnS, the power of the laser was low enough to prevent oxide or sulfate formations. This was also the case for iron-rich sulfides, which can easily form magnetite Fe_3O_4 under strong laser heating. Sulfates and magnetite have strong characteristic Raman bands (Berenblu et al. 1973; De Faria et al. 1997) that were never observed here.

Raman and IR Simulations

First-principles calculations were performed using the density-functional theory (DFT) (Kohn and Sham 1965) and the density-functional perturbation theory (DFPT) (Baroni et al. 2001; Gonze et al. 2002, 2005) in the ABINIT implementation (Gonze et al. 2002, 2005a, 2009; Veithen et al. 2005) with plane waves and norm-conserving pseudopotentials (Troullier and Martins 1991; Payne et al. 1992). We employed a four times shifted 8 × 8 × 8 grid of special k-points (Monkhorst and Pack 1976) for the CaS and MgS endmembers, and

Table 3. Mean compositions obtained by EPMA of typical sulfide phases observed in enstatite meteorites studied in this work.

Sample	Fe	S	Mg	Ca	Cr	Mn	Ti	
(a) in wt%								
Pesyanoe	–	45.11	–	53.33	–	1.56	–	Oldhamite
Pesyanoe	19.14	44.79	–	–	35.63	–	0.45	Daubreelite
Pesyanoe	15.10	37.88	1.14	0.27	–	45.77	–	Alabandite
Pesyanoe	62.06	37.02	–	–	0.50	–	0.43	Troilite
Bustee	14.38	38.55	4.24	–	–	42.83	–	Alabandite
Bustee	62.41	36.76	–	–	–	–	0.83	Troilite
Bustee	–	44.86	–	54.17	–	0.96	–	Oldhamite
Bustee	18.06	44.93	–	–	37.02	–	–	Daubreelite
Zaklodzie	55.67	37.46	–	–	4.75	1.15	0.97	Troilite
Sahara 97158	19.46	46.98	21.72	0.64	–	11.17	–	Niningerite
Sahara 97096	13.33	51.39	25.57	–	–	9.21	–	Niningerite
Aubres	–	44.91	–	55.09	–	–	–	Oldhamite
Aubres	17.59	44.67	–	–	35.93	1.81	–	Daubreelite
Aubres	13.85	39.19	4.9	–	–	41.76	–	Alabandite
Aubres	61.17	36.99	–	–	–	–	1.83	Troilite
El Atchane	16.15	38.47	2.89	0.43	–	42.05	–	Alabandite
El Atchane	59.64	37.39	–	–	2.37	–	0.59	Troilite
Saint Sauveur	35.68	43.84	11.90	1.99	1.85	4.55	–	Keilite
(b) in at%								
Pesyanoe	–	50.87	–	48.11	–	1.03	–	Oldhamite
Pesyanoe	14.08	57.39	–	–	28.15	–	0.38	Daubreelite
Pesyanoe	11.55	50.21	3.33	0.28	–	34.63	–	Alabandite
Pesyanoe	48.65	50.54	–	–	0.42	–	0.39	Troilite
Bustee	10.67	49.81	7.22	–	–	31.09	–	Alabandite
Bustee	48.98	50.26	–	–	–	–	0.76	Troilite
Bustee	–	50.54	–	48.82	–	0.63	–	Oldhamite
Bustee	13.27	57.51	–	–	29.22	–	–	Daubreelite
Zaklodzie	43.39	50.85	–	–	3.97	0.91	0.89	Troilite
Sahara 97158	11.91	50.06	30.53	0.55	–	6.95		Niningerite
Sahara 97096	7.77	52.19	33.89	–	–	6.16	–	Niningerite
Aubres	–	50.47	–	49.53	–	–	–	Oldhamite
Aubres	12.95	57.28	–	–	28.41	1.36	–	Daubreelite
Aubres	10.18	50.17	8.28	–	–	31.35	–	Alabandite
Aubres	47.89	50.44	–	–	–	–	1.67	Troilite
El Atchane	12.13	50.32	4.99	0.45	–	32.11	–	Alabandite
El Atchane	46.59	50.87	–	–	1.99	–	0.54	Troilite
Saint Sauveur	23.4	50.69	18.00	2.05	1.5	3.15	–	Keilite

correspondingly smaller for supercells. We used several supercells along the (Ca,Mg)S solid solution to study the effect of the chemical composition on the Raman spectra. We employed a 38 Hartrees (1Hartree = 27.2116 eV) cutoff for the kinetic energy. For the ZnS calculations, we used 40 Hartree cutoffs (for consistency with other WURM calculations) and 6 × 6 × 6 grids of special k-points. We determined the Raman spectra, with both peak position and intensity, in the framework of DFPT. For more details, the reader is encouraged to check the WURM database description (Caracas and Bobocioiu 2011) or the original paper on the implementation (Veithen et al. 2005).

RESULTS

General Features of the Sulfide Assemblages

Meteorite Samples

Oldhamite, niningerite, keilite, alabandite, and daubreelite are generally found in close association with troilite and kamacite (Fig. 1) (e.g., Keil 1968, 1989, 2007; Brearley and Jones 1998). Grains of oldhamite and alabandite are sometimes observed outside of the metal, in the enstatite matrix, e.g., in Aubres or Bustee (Fig. 1). Some sulfide grains are well defined with homogeneous major element compositions as in Zaklodzie, Pesyanoe,

Table 4. Mean compositions of the sulfide phases (in wt%) obtained by EPMA for the piston-cylinder samples.

Sample	Fe	Si	S	Mg	Ca	Cr	Mn	V	Nd
ENS#1	34.45	0.40	44.97	17.80	1.28	0.39		0.60	–
#151	2.08	–	59.80	35.07 ± 0.7	2.89	0.10	0.20	0.25	–
#154	16.12	2.72	47.80	22.05 ± 0.9	9.89	–	0.2	0.35	–
#ENS 3-1	18.32	0.10	48.11	13.20	19.12	–	0.88	0.37	–
#ENS 3-1	59.90	–	37.64	0.36	–	–	–	2.03	–
#ENS 3-2	5.42	–	54.23	22.82	16.00	–	0.08	0.76	–
#ENS 8	30.29	–	46.34	16.10	7.03	–	–	–	–
#ENS 8	61.83	–	37.53	–	–	–	–	–	–
#ENS 204	27.73	–	47.82	20.24	3.92	–	0.20	–	–
#ENS 204	63.79	–	36.21	–	–	–	–	–	–
#242	25.4	0.29	48.14	16.32	5.84	0.86	1.7	0.64	–
#170	14.42	–	50.46	27.03	7.40	–	–	0.33	–
#ENS 5-1	61.90	–	35.70	–	–	–	0.35	1.14	–
#ENS 5-1	2.75	0.15	44.19	3.07	43.09	–	–	–	5.38
#ENS 5-1	17.90	0.29	47.22	16.44	16.26	–	–	1.12	0.17
#ENS 5-2	2.86	0.54	44.49	12.17	32.85	–	0.4	0.42	6.48
#ENS 5-2	4.50	0.10	51.22	26.23	11.82	–	0.60	1.54	2.24

Aubres, Bustee (Figs. 1a–c). They can host occasionally planar, or roughly spherical sulfides or metal grains (Fig. 1e). Similar observations were already reported in the literature (e.g., Keil 1968, 2007; Brearley and Jones [1998] and references therein) and interpreted as the result of the cooling history of the meteorite. The sulfide compositions were generally homogeneous in the aubrites studied here, but more variable in the enstatite chondrites. Average chemical compositions of the sulfide minerals in the meteorite samples investigated in this study are listed in Table 3. The Raman spectroscopic data were collected in homogeneous sulfide grains, or far from heterogeneities (i.e., far from sulfides exsolutions like daubreelite in Fig. 1e).

High-Pressure Synthetic Samples

The chemical and textural details of the synthetic samples are found in Malavergne et al. (2012). The silicate phases are pyroxene and quenched melt, depending on the run temperature. Evidence for silicate melt is seen above 1350 °C. The metal phase contains Si, as in enstatite meteorites, showing that heating took place in reducing conditions.

The textures of the sulfide assemblages are similar to those observed in meteorites. The sulfides (oldhamite or niningerite) occur in close association with troilite and metal (Fig. 2). Grains of oldhamite or niningerite were also found in the silicate matrix without connection to metal or troilite (Fig. 2), like in enstatite meteorites. The niningerite compositions (Table 4) are close to that of natural niningerite, whereas synthetic oldhamite compositions are generally different from those of natural oldhamite ones. Our synthetic troilite has a very low Cr content and no Ti, unlike natural troilites in the enstatite meteorites studied here, because the experimental starting materials contained no Ti and only a little Cr (less than 0.1 wt%). Sulfide compositions, just like those of the two other phases (silicate and metal), are homogeneous, except for the samples that were subjected to slow cooling (see Table 2) in which small chemical heterogeneities could be observed. Chemical homogeneity demonstrates attainment of equilibrium during the constant temperature stage of the experiments.

Raman Spectra

Oldhamite, Ca-Rich Sulfide

Figure 3 shows the room temperature Raman spectra of oldhamite. Both synthetic and natural samples exhibit low-frequency peaks at 160, 185, 205, and 285 cm^{-1} for all spectra. The spectra of $(Ca_{0.60}$ $Mg_{0.36}$ $Fe_{0.04})S$ found in the sample #ENS5-2 (Fig. 3a) differ noticeably from the other three (Figs. 3b–d). We observed four peaks in this spectrum at 160, 225, 290, and 360 cm^{-1}. We believe this to be due to an overlap of the 185 and 205 cm^{-1} peaks, by a first Raman line at 225 cm^{-1} in the spectra of $(Ca_{0.60}$ $Mg_{0.36}$ $Fe_{0.04})S$. To obtain Raman spectra of the same quality as for natural oldhamite (Fig. 3b), it was necessary to perform a high-pressure sintering (piston cylinder) of the commercial CaS powder. The Raman peak positions of these Ca-rich sulfides are summarized in Table 5.

Niningerite, Mg-Rich Sulfide

The Raman spectra of natural niningerites have two characteristic bands at 225 and 285 cm^{-1} (Fig. 4). The intensity of the Raman peak at 225 cm^{-1} is enhanced by

Table 5. Raman peak positions (in cm^{-1}) observed for the different sulfides of this study. These Raman peaks are compared to the calculated frequencies for the Ca-rich sulfides and Mg-rich sulfides. We found that inactive or infrared-active vibrational modes become Raman active through local symmetry breaking. Some Raman peaks are in agreement with the calculated frequencies (in bold). These comparisons suggest strongly that the first observed Raman peak (around 160 cm^{-1}) is mainly due to symmetry breaking (cf. Table 6).

Oldhamite		Niningerite		Troilite		Alabandite		Daubreelite
CaS	CaS- (Ca, Mg,Fe)S	MgS	MgS-(Mg, Fe,Ca)S	FeS	FeS-(Fe, Mg,Ca)S	MnS-(Mn, Fe, Mg)S	Cr_2S_3	$FeCr_2S_4$
160	**160**	165	**165**	160	160	160	160	160
185	**185**							
215 (±15)	**215 (±15)**		**225**		240[a]	230	255	255
285 (±10)	**285 (±10)**	**285**	**285**		290	285	290	290
			310[a]	310				
350 (±10)[a]			**360**[a]	360	335		365	
485 (±10)[a]	485 (±10)[a]	**470**	470[a]					
						580[a]		

[a]Peak not always present.

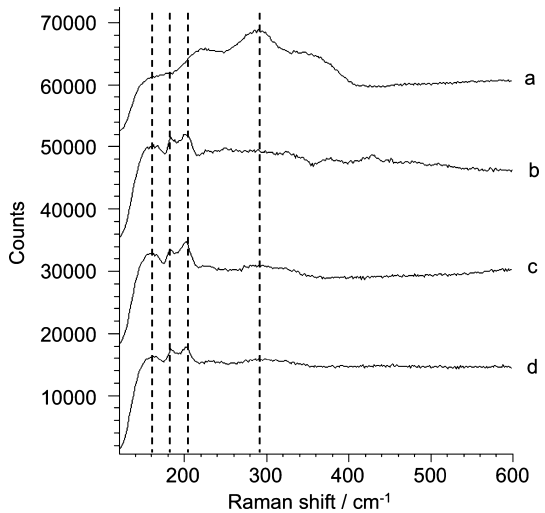

Fig. 3. Raman spectra of synthetic and natural oldhamite in the 40–590 cm^{-1} region (a) $(Ca_{0.60}\ Mg_{0.36}\ Fe_{0.04})S$ found in #ENS5-2, (b) pure CaS obtained in sample #ENS180, (c) and (d) natural oldhamites from Pesyanoe and Bustee meteorites, respectively. The same spectra were obtained from El Atchane and Saint Sauveur.

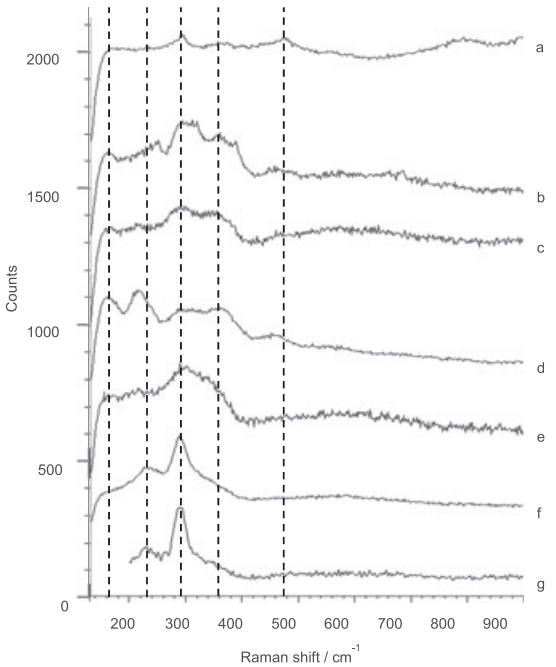

Fig. 4. Raman spectra of synthetic and natural niningerite in the 70–990 cm^{-1} range. (a) Pure MgS in sample #ENS3-3, (b) $(Mg_{0.71}\ Fe_{0.17}\ Ca_{0.12})S$ in sample #170, (c) $(Mg_{0.63}\ Fe_{0.20}\ Ca_{0.17})S$ in sample #154, (d) $(Mg_{0.92}\ Ca_{0.05}\ Fe_{0.02})S$ in sample #151, (e) $(Mg_{0.40}\ Ca_{0.35}\ Fe_{0.24}\ Mn_{0.01})S$ in #ENS3-1 (f) $(Mg_{0.73}\ Fe_{0.16}\ Mn_{0.11})S$ found in Sahara 97096.

the presence of iron in the solid solution. We observed the same Raman peaks for synthetic niningerite with additional Raman bands at 360 and 470 cm^{-1}. The Raman peaks with the highest frequency, at 360 and 470 cm^{-1}, decrease in intensity or even disappear when the Fe concentration increases. Previous Raman measurements performed on $(Mg_{0.92}\ Fe_{0.04}\ Ca_{0.03}\ Mn_{0.01})S$ (Siebert et al. 2004) yielded similar spectra with bands around 220, 360, 470, and 650 cm^{-1}, and the main peak at 290 cm^{-1}. The Raman peak positions of these Mg-rich sulfides are summarized in Table 5.

Troilite, FeS Sulfide

The room temperature Raman spectra of troilite display three peaks at 160, 290, and 335 cm^{-1} (Fig. 5). The peaks at 160 and 290 cm^{-1} are not always observed. The peak at 335 cm^{-1} is slightly shifted in the spectrum obtained from a synthetic powder of troilite.

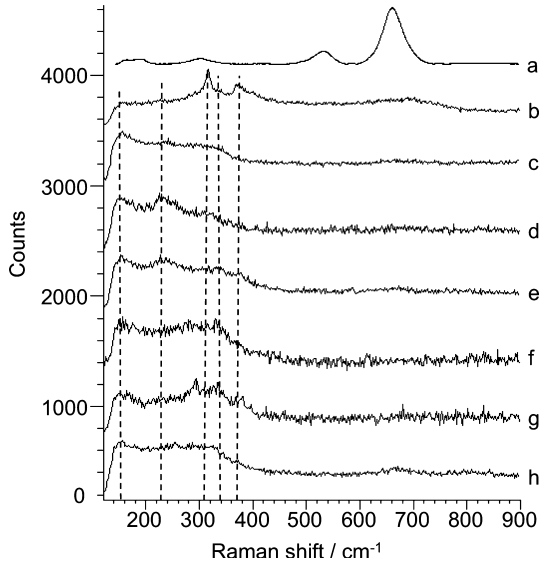

Fig. 5. Raman spectra of synthetic and natural troilite in 70–990 cm^{-1} region from a) Raman spectra of natural magnetite has been added to show that no magnetite formed during this spectroscopic Raman work. b) pure synthetic powder of FeS, c) FeS in #ENS5-1, d) FeS in #ENS3-1, e) FeS in #ENS3-2, f) FeS in #ENS3-1, and grains of natural troilite in: g) Bustee, h) Aubres, and i) Sahara 97158; the same spectra were obtained with El Atchane and Zaklodzie.

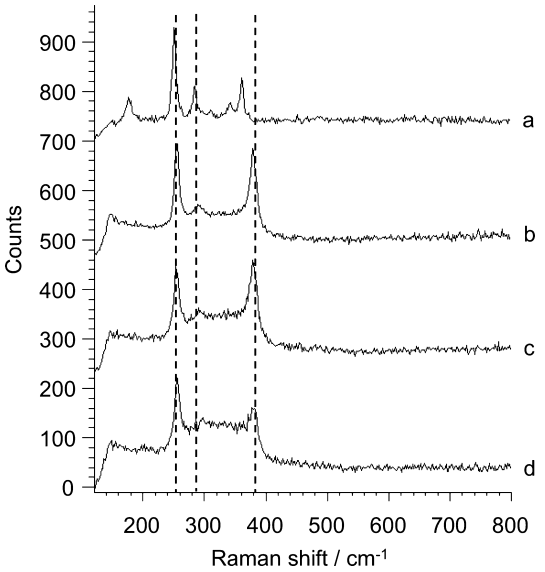

Fig. 6. Raman spectra in the 70–960 cm^{-1} range for synthetic Cr_2S_3 powder a) and natural daubreelites $FeCr_2S_4$ in b) Bustee, c) Pesyanoe, and d) Aubres meteorites; the same spectra were obtained with El Atchane and Saint Sauveur.

We also observed a new Raman peak at 240 cm^{-1} in spectra (Figs. 5c and 5d) collected on synthetic troilite from piston-cylinder experiments (#ENS3-1 and #ENS5). It is worth mentioning that collecting good quality spectra for troilite was difficult, both on synthetic powders and on natural or synthetic large grains. This is probably due to a strong laser absorption by iron sulfides, but it cannot be attributed to the oxidation of troilite into magnetite (Fig. 5). The Raman peak positions of these Fe-rich sulfides are summarized in Table 5.

Daubreelite $FeCr_2S_4$ and Cr_2S_3

The spectra of natural daubreelite (Fig. 6) in the Bustee (a), Pesyanoe (b), and Aubres (c) meteorites all exhibit peaks at 160, 255, 290, and 365 cm^{-1}. We observed the same spectra for daubreelite in the El Atchane and Sahara meteorites. A Raman peak is also observed at 550 cm^{-1} in the spectrum of pure Cr_2S_3 powder. The Raman peak positions of these Cr-rich sulfides are summarized in Table 5.

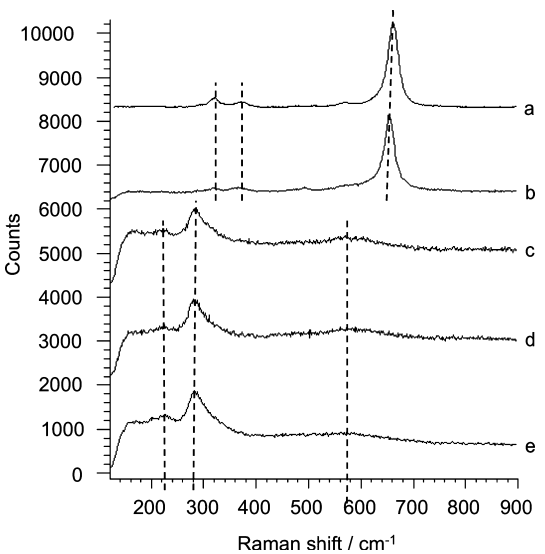

Fig. 7. Raman spectra of synthetic and Mn-rich sulfides or oxides in the 70–990 cm^{-1} range a) natural hausmannite Mn_3O_4, b) synthetic powder of pure MnS converted into hausmannite during laser heating, which was not the case with natural alabandite, c) $(Mn_{0.64}\ Fe_{0.21}\ Mg_{0.15})S$ in Bustee, d) $(Mn_{0.72}\ Fe_{0.23}\ Mg_{0.04}\ Ca_{0.01})S$ in Pesyanoe, e) $(Mn_{0.74}\ Fe_{0.22}\ Mg_{0.04})S$ in Bustee; the same spectra were obtained with El Atchane, Saint Sauveur, and Sahara 97158.

Alabandite, Mn-Rich Sulfide

The Raman spectrum of synthetic MnS powder corresponds to the peaks of hausmannite, showing that a conversion of MnS into Mn_3O_4 (the main peak around 655 cm^{-1} with additional low-intensity peaks around 250 and 370 cm^{-1}) occured during laser heating only for this sample, as it is shown in Figs. 7a and 7b. The spectra of natural alabandite exhibit peaks at 230 and 285 cm^{-1} (Figs. 7c and 7d). The Raman peak

Table 6. Calculated frequencies (in cm^{-1}). According to group theory, in ideal ordered samples, the frequencies of MgS and CaS are all infrared-active, but silent in Raman. Local symmetry breaking, due to clustering and disorder relation, activates some of these modes in Raman (in italic and underlined). There is a good agreement between the experimental infrared spectra and particular computed modes along the solid solution. The Raman frequencies observed for the Mg-rich and Ca-rich sulfides of this study (cf. Table 5) are in bold.

MgS IR (Kimura et al. 2005)	MgS	$Mg_{0.875}Ca_{0.125}S$	$Mg_{0.75}Ca_{0.25}S$	$Mg_{0.25}Ca_{0.75}S$	$Mg_{0.125}Ca_{0.875}S$	CaS
				75 (TO)		
		123	112–113	113	117	
				118 (LO)		
		126	121	122 (TO)	121	
				150 (LO)	148	
		158			**154 (TO)-158** (LO)	
		169	173	178 (TO)	179	
		182		181 (LO)	**186**	
		192	191		189	
		194				
		217	203		202 (TO)	
					222 (LO)-225	
		232 (TO)	236		229	
250	255 (TO)	248			243	**252** (TO)
262		*261*				
		271 (LO)-273 (TO)			272 (TO)	
		283		286 (TO)	**283–285–289** (TO)	
				299	290 (LO)-298 (TO)	
				308 (LO)		
311		**327** (LO)- *332*	319 (LO)	311 (TO)		
		352–353				**356** (LO)
		356		372 (LO)	364 (LO)	
400	406 (LO)	406	396			
			426			
460						

positions of these Mn-rich sulfides are summarized in Table 5.

Theoretical Spectra of ZnS and (Mg,Ca)S

The results obtained from the simulations on several ordered terms along the MgS-CaS solid solution are summarized in Table 6. The MgS and CaS endmembers have one T_u, triply degenerated, IR-active mode, and no Raman-active mode. For the solid solution, we considered various ordered configurations with 7:1 and 3:1 cation ratios. Our calculations showed that the associated symmetry breaking due to ordering and clustering removes the T_u degeneracy and yielded both infrared and Raman-active modes. In general, our calculations are in good agreement with the measurements on almost pure phases (Kaneko et al. 1982; Kimura et al. 2005). Both calculations and measurements for the intermediate members of the solid-solution series are more difficult to compare, as explained in the following section. Theoretical results on the two ZnS polymorphs are discussed below in the text.

DISCUSSION

None of the cubic ideal endmember terms, MgS, CaS, and MnS, are Raman active because of the *Fm3 m* symmetry of the rocksalt structure. However, each monosulfide is in reality a complex solid solution in which the major substituting cations are Ca, Mg, Mn, and Fe (e.g., Skinner and Luce 1971). These chemical substitutions promote domain formation, ordering, and clustering that lead to symmetry breaking. As a result, normally inactive or infrared-active vibrational modes become Raman active through local symmetry breaking as seen in Figs. 3, 4, and 7 and as shown by calculations on ordered solid solutions (Tables 5 and 6). In some particular cases, it is then possible to describe the way in which the substituting cations Mg, Ca, Mn, or Fe modify the Raman spectra of pure sulfides: CaS, MgS, MnS, FeS. Similar attempts have been already performed, but at a more limited scale. For example, crystallographic defects (sulfur and calcium vacancies) have been characterized in CaS (Auzins et al. 1963; Ghosh and Pandey 1982). Ravindra and Sivaraman

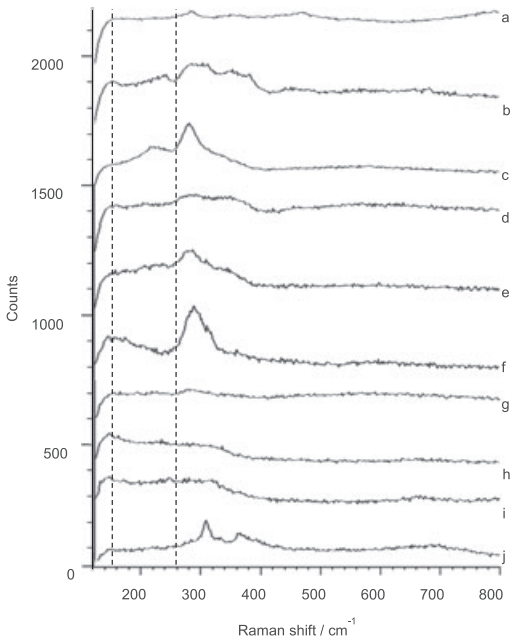

Fig. 8. Raman spectra of (a) pure MgS in sample #ENS3-3 (b) $(Mg_{0.71}\ Fe_{0.17}\ Ca_{0.12})S$ in sample #170, (c) $(Mg_{0.73}\ Fe_{0.16}\ Mn_{0.11})S$ in Sahara 97158 (d) $(Mg_{0.63}\ Fe_{0.20}\ Ca_{0.17})S$ grain from sample #154, (e) $(Mg_{0.53}\ Fe_{0.44}\ Ca_{0.02})S$ grain in sample ENS1 (f) $(Mg_{0.37}\ Fe_{0.47}\ Ca_{0.05}\ Mn_{0.07}\ Cr_{0.04})S$ in Saint Sauveur, (g) $(Mg_{0.32}\ Fe_{0.60}\ Ca_{0.14})S$ in sample ENS204, (h) FeS in sample ENS3-2, (i) grains of natural troilite in Sahara 97158, (j) FeS powder.

(1991) reviewed results of spectroscopic studies on sulfides (particularly CaS and MgS) and showed how intrinsic defects and impurities alter their physical properties. Raman-inactive vibrational modes of sulfides may become Raman active because of coupling with electronic transitions in the Fe- and Mn-rich sulfides semiconductor materials. Finally, Siebert et al. (2004) recorded Raman spectra of $(Mg_{0.92}\ Fe_{0.04}\ Ca_{0.03}\ Mn_{0.01})S$ sulfides synthesized at 20–25 GPa and 2000–2200 °C. As these niningerite-like sulfides should not have a first-order Raman spectrum at ambient conditions, they interpreted their results by high-pressure polymorph of niningerite. The present work shows that no polymorphism needs to be invoked to explain these observations.

Figure 8 illustrates the Raman spectra of the (Mg, Fe, Ca)S solid solution for various Fe concentrations. Due to the systematic presence of Ca, it is impossible to isolate just the effect of Mg and Fe. However, we observed that the Mg-rich sulfide component has a main broad Raman frequency domain in the 285–300 cm^{-1} range, and a second set of modes around 470 cm^{-1}. The increase in iron concentration is correlated with a decrease in intensity of the high-frequency Raman bands, and with a relative increase of the frequencies below about 160 cm^{-1}. The experimental Raman spectra exhibit many of the IR-active peaks predicted by DFT, suggesting that the IR modes are activated by the above-mentioned local symmetry breaking mechanism. For example, the 160 cm^{-1} mode is observed only within the (Mg, Fe, Ca)S solid solution and not in the endmember terms. White (2009) published different Raman spectra of sulfides and elemental sulfur. They found that orthorhombic sulfur, S_8, has two main Raman modes at 219 and 472 cm^{-1} with other Raman-active modes at 153, 187, 219, 246, 437, and 472 cm^{-1}. They attributed the 100–300 cm^{-1} bands to S-S-S bending and the bands in the 400–500 cm^{-1} region to S-S stretching. Sphalerite (Zn,Fe)S (cubic, F43 m) exhibits similar features, with bands at 298, 329, 340, and 350 cm^{-1}. Calculations on pure ZnS sphalerite yielded one Raman-active peak with Tg symmetry at 288 cm^{-1}. Again Zn/Fe ordering in the solid solution lifts the degeneracy of the Tg mode. The spectra of synthetic wurtzite, (Zn, Fe)S (hexagonal, $P6_3mc$) show bands at 294, 308, 326, 352, and 1167 cm^{-1}. First-principles calculations on ZnS wurtzite showed a series of strong Raman peaks at 287, 291, and 296 cm^{-1}, corresponding to Fe-S vibrations. An infrared mode was computed at 346 cm^{-1}. We could attempt to assign the low-frequency experimental Raman modes to Fe-S vibrations and the experimental band at 470 cm^{-1} to an Mg-S stretching mode.

For Ca-rich sulfides, the main Raman peaks occur at 160, 185, and 215 cm^{-1}. The infrared (IR) spectra of CaS and MgS have been measured and show one peak at 250 cm^{-1} for CaS (Kaneko et al. 1982) and two peaks at 311 and 250 cm^{-1} for MgS (Kimura et al. 2005). These results are in good agreement with our calculations, which yielded E_u peaks at 252 and 255 cm^{-1}, respectively, for CaS and MgS. The 311 cm^{-1} peak was observed in calculations for the Mg-rich members (Table 6). Pandey and Sivaraman (1991) suggested that the optical phonon in CaS could be treated as the central-force model as a classical oscillator model yielded a phonon frequency of about 229 cm^{-1}. A series of peaks is predicted by theory to occur at lower frequency, below 200 cm^{-1}. Again, their occurrence is interpreted as the result of symmetry breaking due to ordering in the solid solution, or phonon-electron coupling.

This first Raman database constitutes a starting point for the identification of sulfides found in enstatite meteorites, and more generally in reduced sulfur-rich chemical systems. The Mg-rich sulfides or niningerite-like sulfides have two main characteristic frequencies (360 and 470 cm^{-1}). The Ca-rich sulfides or oldhamite-like sulfides have three main frequencies (185, 215, and 285 cm^{-1}), which can be assigned obviously to a CaS contribution only. The Mn-rich sulfides or alabandite-like sulfides

have three main frequencies (230, 270, and 580 cm^{-1}) in alabandites from meteorites. The Cr-rich sulfides or daubreelite-like sulfides have three main characteristic frequencies (255, 290, and 365 cm^{-1}). The Fe-rich sulfides or troilite-like sulfides have three main frequencies (160, 290, and 335 and sometimes 240 cm^{-1}), but troilite remains the most difficult sulfide phase to identify with this method. In almost all the Raman spectra, the 160 cm^{-1} frequency was present and could not be used to discriminate between the different sulfide compositions.

Acknowledgments—The center for Raman spectroscopy at ENS Lyon is supported by INSU. Part of this research has been funded by the Programme National de Planétologie (CNRS-INSU).

Editorial Handling—Dr. Michael Zolensky

REFERENCES

Auzins A., Ortan J. W., and Wert J. E. 1963. *Paramagnetic resonance*, vol. 1. New York: Academic Press. 90 p.

Baroni S., de Gironcoli S., Dal Corso A., and Giannozzi P. 2001. Phonons and related crystal properties from density-functional perturbation theory. *Reviews of Modern Physics* 73:515–562.

Berenblu B. J., Dawson P., and Wilkinso G. G. 1973. Comparison of Raman-spectra of anhydrite ($CaSO_4$) and gypsum ($CaSO_4.2H_20$). *Spectrochimica Acta A* 29:29–36.

Brearley A. J. and Jones R. H. 1998. Chondritic meteorites. In *Planetary materials*, edited by Papike J. Reviews in Mineralogy, vol. 36. Washington, D.C.: Mineralogical Society of America. pp. 250–398.

Brunet F., Bagdassarov N., and Miletich R. 2003. $Na_3Al_2(PO_4)_3$, a fast sodium conductor at high pressure: In-situ impedance spectroscopy characterisation and phase diagram up to 8 GPa. *Solid State Ionics* 159:35–47.

Caracas R. and Bobocioiu E. 2011. The WURM project—A freely available web-based repository of computed physical data for minerals. *American Mineralogist* 96:437–444.

De Faria D. L. A., Venancio Silva S., and de Oliveira M. T. 1997. Raman microspectroscopy of some iron oxides. *Journal of Raman Spectroscopy* 28:873–878.

Farquhar J., Wing B. A., McKeegan K. D., Harris J. W., Cartigny P., and Thiemens M. H. 2002. Mass-independent sulfur of inclusions in diamond and sulfur recycling on early Earth. *Science* 298:2369–2372.

Farrell S. P., Fleet M. E., Stekhin I. E., Kravtsova A., Soldatov A. V., and Liu X. 2002. Evolution of local electronic structure in alabandite and niningerite solid solutions (Mn,Fe)S, (Mg,Mn)S, (Mg,Fe)S using sulfur K- and L-edge XANES spectroscopy. *American Mineralogist* 87:1321–1332.

Filiberto J., Treiman A., and Le L. 2008. Crystallization experiments on a Gusev Adirondack Basalt Composition. *Meteoritics & Planetary Science* 43:1137–1146.

Gaillard F. and Scaillet B. 2009. The sulfur content of volcanic gases on Mars. *Earth and Planetary Science Letters* 270:34–43.

Ghosh P. K. and Pandey R. 1982. Thermoluminescence due to intrinsic point defects in polycrystalline calcium sulphide. *Journal of Physics C* 15:5875.

Gonze X., Beuken J. M., Caracas R., Detraux F., Fuchs M., Rignanese G. M., Sindic L., Verstraete M., Zerah G., Jollet F., Torrent M., Roy A., Mikami M., Ghosez Ph., Raty J. Y., and Allan D. C. 2002. First-principle computation of material properties the ABINIT software project. *Computational Materials Science* 25:478–492.

Gonze X., Rignanese G. M., Verstraete M., Beuken J. M., Pouillon Y., Caracas R., Jollet F., Torrent M., Zerah G., Mikami M., Ghosez Ph., Veithen M., Raty J. Y., Olevano V., Bruneval F., Reining L., Godby R., Onida G., Hamann D. R., and Allan D. C. 2005a. A brief introduction to the ABINIT software package. *Zeitschrift für Kristallographie* 220:558–562.

Gonze X., Rignanese G. M., and Caracas R. 2005b. First-principles studies of the lattice dynamics of crystals, and related properties. *Zeitschrift für Kristallographie* 220:458–472.

Gonze X., Amadon B., Anglade P. M., Beuken J. M., Bottin F., Boulanger P., Bruneval F., Caliste D., Caracas R., M. Côté, Deutsch T., Genovesi L., Ghosez Ph., Giantomassi M., Goedecker S., Hamann D. R., Hermet P., Jollet F., Jomard G., Leroux S., Mancini M., Mazevet S., Oliveira M. J. T., Onida G., Pouillon Y., Rangel T., Rignanese G. M., Sangalli D., Shaltaf R., Torrent M., Verstraete M. J., Zerah G., and Zwanziger J. W. 2009. ABINIT: First-principles approach to material and nanosystem properties. *Computer Physics Communications* 180:2582–2615.

Grossmann J. N. 2000. The Meteoritical Bulletin, No. 84. *Meteoritics & Planetary Science* 35:A199–A225.

Grossmann J. N. and Zipfel J. 2001. The Meteoritical Bulletin, No. 85. *Meteoritics & Planetary Science* 36:A293–A322.

Holzheid A. and Grove T. L. 2002. Sulfur saturation limits in silicate melts and their implications for core formation scenarios for terrestrial planets. *American Mineralogist* 87:227–237.

Kaneko Y., Morimoto K., and Koda T. 1982. Optical properties of alkaline-Earth chalcogenides in single crystal growth and infrared reflection spectra due to optical phonons. *Journal of the Physical Society of Japan* 51:2247–2254.

Keil K. 1968. Mineralogical and chemical relationships among enstatite chondrites. *Journal of Geophysical Research* 73:6945–6976.

Keil K. 1989. Enstatite meteorites and their parent bodies. *Meteoritics* 24:195–208.

Keil K. 2007. Occurrence and origin of keilite, $(Fe_{>0.5}, Mg_{<0.5})S$, in enstatite chondrite impact-melt rocks and impact-melt breccias. *Chemie der Erde* 67:37–54.

Keil K. 2010. Enstatite achondrite meteorites (aubrites) and the histories of their asteridal parent bodis. *Chemie der Erde* 70:295–317.

Kimura Y., Kurumada M., Tamura K., Koike C., Chihara H., and Kaito C. 2005. Laboratory production of magnesium sulfide grains and their characteristic infrared spectra due to shape. *Astronomy & Astrophysics* 442:507–512.

Kohn W. and Sham L. J. 1965. Self-consistent equations including exchange and correlation effects. *Physical Review* 140:A1133–A1138.

Kong P., Mori T., and Ebihara M. 1997. Compositional continuity of enstatite chondrites and implications for

heterogeneous accretion of the enstatite chondrite parent body. *Geochimica et Cosmochimica Acta* 61:4895–4914.

Lauretta D. S., Lodders K., and Fegley B., Jr. 1997. Experimental simulations of sulfide formation in the solar nebula. *Science* 277:358–360.

Liu Y., Samaha N.-T., and Baker D. R. 2007. Sulfur concentration at sulfide saturation (SCSS) in magmatic silicate melts. *Geochimica et Cosmochimica Acta* 71:1783–1799.

Malavergne V., Tarrida M., Combes R., Bureau H., J. Jones, and Schwandt C. 2007. New high-pressure and high-temperature metal/silicate partitioning of U and Pb: Implications for the cores of the Earth and Mars. *Geochimica et Cosmochimica Acta* 71:2635–2655.

Malavergne V., Brunet F., Righter K., Zanda B., Avril C., Borensztajn S., and Berthet S. 2012. Experimental behavior of sulfur under primitive planetary differentiation processes, the sulfide formations in enstatite meteorites and implications for Mercury (abstract #1873). 43rd Lunar and Planetary Science Conference. CD-ROM.

McCoy T. J., Dikinson T. L., and Lofgren G. E. 1999. Partial melting of the Indarch (EH4) meteorite: A textural, chemical, and phase relation view of melting and melt migration. *Meteoritics & Planetary Science* 34:735–746.

McDade P., Wood B. J., Van Westrenen W., Brooker R., Gudmundsson G., Soulard H., Najorka J., and Blundy J. 2002. Pressure correction for a selection of piston-cylinder cell assemblies. *Mineralogical Magazine* 66:1021–1028.

McMillan P. F. and Hofmeister A. M. 1988. Infrared and Raman spectroscopy. In *Spectroscopic methods in mineralogy and geology*, edited by Hawthorne F. C. Reviews in Mineralogy, vol. 18. Washington, D.C.: Mineralogical Society of America. pp. 99–160.

Monkhorst H. J. and Pack J. D. 1976. Special points for Brillouin-zone integrations. *Physical Review* B13:5188–5192.

Moretti R. and Ottonello G. 2005. Solubility and speciation of sulfur in silicate melts: The conjugated toop-samis-flood-grjotheim (CTSFG) model. *Geochimica et Cosmochimica Acta* 69:801–823.

Musselwhite D. S., Dalton H. A., Keifer W. H., and Treiman A. H. 2006. Experimental petrology of the basaltic Shergottite Yamato 980459: Implications for the thermal structure of the Martian mantle. *Meteoritics & Planetary Science* 41:1271–1290.

Pandey R. and Sivaraman S. 1991. Spectroscopic properties of defects in alkaline-earth sulfides. *Journal of Physics and Chemistry of Solids* 52:211–225.

Pasek M. A., Milsom J. A., Ciesla F. J., Lauretta D. S., Sharp C. M., and Lunine J. I. 2005. Sulfur chemistry with time-varying oxygen abundance during solar system formation. *Icarus* 175:1–14.

Patzer A., Hill D. H., and Boynton W. V. 2001. Itqiy: A metal-rich enstatite meteorite with achondritic texture. *Meteoritics & Planetary Science* 36:1495–1505.

Patzer A., Hill D. H., Boynton W. V., Franke L., Schultz L., Jull A. J. T., McHargue L. R., and Franchi I. A. 2002. Itqiy: A study gases and oxygen isotope including its terrestrial age and composition with Zaklodzie. *Meteoritics & Planetary Science* 37:823–833.

Payne M. C., Teter M. P., Allan D. C., Arias T. A., and Joannopoulos J. D. 1992. Iterative minimization techniques for ab initio total-energy calculations: Molecular dynamics and conjugate gradients. *Reviews of Modern Physics* 64:1045–1097.

Ravindra P. and Sivaraman S. 1991. Spectroscopic properties of defects in alkaline-earth sulfides. *Journal of Physics and Chemistry of Solids* 52:211–225.

Sears D. W. G., Kallemeyn G. W., and Wasson J. T. 1982. The compositional classification of chondrite-II. The enstatite chondrite groups. *Geochimica et Cosmochimica Acta* 46:597–608.

Siebert J., Malavergne V., Guyot F., Combes R., and Martinez I. 2004. The behaviour of sulphur in metal-silicate core segregation experiments under reducing conditions. *Physics of the Earth and Planetary Interiors* 143–144:433–443.

Sinyakavo E. F. and Kosyakov V. I. 2001. 600 °C section of the Fe-FeS-NiS-Ni phase diagram. *Inorganic Materials* 37:1130–1137.

Skinner B. J. and Luce F. D. 1971. Solide solutions of the type (Ca, Mg, Mn, Fe)S and their use as geothermometers for the enstatite chondrites. *American Mineralogist* 56:1269–1296.

Soong R. and Farmer V. C. 1978. The identification of sulfide minerals by infrared spectroscopy. *Mineralogical Magazine* 42:M17–M20.

Toplis M. J. and Reynard B. 2000. Temperature and time-dependent changes of structure in phosphorus containing aluminosilicate liquids and glasses: In situ Raman spectroscopy at high temperature. *Journal of Non-Crystalline Solids* 263–264:123–131.

Troullier N. and Martins J. L. 1991. Efficient pseudopotentials for plane-wave calculations. *Physical Review B* 43:1993–2006.

Veithen M., Gonze X., and Ghosez P. 2005. Non-linear optical susceptibilities, Raman efficiencies and electrooptic tensors from first-principles density functional perturbation theory. *Physical Review* 71:125107.

Wang A., Jolliff B. L., and Haskin L. A. 1999. Raman spectroscopic characterization of a Martian SNC meteorite: Zagami. *Journal of Geophysical Research* 104:8509–8519.

Weber W. H. and Merlin R. 2000. *Raman scattering in materials science*. New York: Springer. 492 p.

White S. N. 2009. Laser Raman spectroscopy as a technique for identification of seafloor hydrothermal and cold minerals. *Chemical Geology* 259:240–252.